

Gas heating by radiation absorbing inertial particles in a turbulent duct flow

By L. Villafañe, A. Banko, C. Elkins AND J. K. Eaton

1. Motivation and objectives

Preferential concentration is encountered in a wide range of particle-laden flows in which inertial particles are transported by turbulence. The response of the particles to the carrier turbulent fluctuations depends on their relative time scale, or Stokes number. A consequence of inertial particles not able to follow all the rapid flow fluctuations is their accumulation in regions of high shear, leaving devoid zones of strong vorticity (Maxey 1987; Squires & Eaton 1991). Much of the research on particle clustering is motivated by cloud physics, as concentration fluctuations enhance particle collisions and coalescence, consequently affecting droplet growth and precipitation (Sundaram & Collins 1997; Kostinski & Shaw 2001). Number density fluctuations can also be a source of inhomogeneities in the system such as temperature or reaction rate fluctuations. Spray and coal combustion, slurry catalysis, and enhanced heat-transfer fluids, where the disperse phase acts as localized sources of heat and mass transfer in industrial flows that are typically turbulent, are a few examples of such systems (Williams 1958; Brian *et al.* 1969; Kuerten *et al.* 2011). In addition, correlations in particle positions affect radiation transfer and radar reflection in clouds (Shaw *et al.* 2002; Matsuda *et al.* 2014).

Particle-based solar receivers use solid particles dispersed in an optically transparent carrier fluid to absorb concentrated solar radiation. Different types of receivers are under development that depend on the form of the thermal carrier. When the fluid is used as thermal carrier, the particles volumetrically heat the working fluid, minimizing the energy losses due to surface re-radiation that penalize conventional surface absorbers (Lenert & Wang 2012). The design of this type of receiver is challenged by the presence of inhomogeneities in particle number density that simultaneously affect the radiation transmission through the particle-fluid mixture and cause fluctuations in the thermal field. Several experimental (Klein *et al.* 2008; Kim *et al.* 2009; Bertocchi *et al.* 2004) and numerical (Miller & Koenigsdorff 2000; Chen *et al.* 2007; Crocker & Miller 2011) studies investigated the use of solid particles in solar receivers for various applications such as gas process, methane decomposition or solar-powered gas turbines systems for electricity generation. All these studies neglected instantaneous turbulent fluctuations of the carrier phase, therefore ignoring their effect on the performance of these devices.

The efficiency of a particle-based solar receiver depends on the coupling between radiation, particles and turbulence. The significance of the coupling effects depends on a set of design and operational parameters such as particle material and size, volume fraction, and working fluid. The exchange of momentum between a turbulent fluid and particles may lead to the dynamic formation of particle clusters and voids, and also to the modulation of the turbulent field (Fessler *et al.* 1994). In a radiation environment particles absorb the thermal energy and heat the surrounding fluid that is otherwise transparent to radiation. The existence of large voids and partially shadowed particles can reduce the total amount of radiation absorbed in the system (Matsuda *et al.* 2012) while cre-

ating local hot spots in regions with high particle concentrations. Fluid temperature fluctuations can have a detrimental effect on downstream power-generation components (Yapa *et al.* 2015; Casaday *et al.* 2014), and if the energy input from radiation is large enough, buoyancy effects can become important by altering the turbulent field and affecting the redistribution of particles in the flow (Zamansky *et al.* 2014). Recent studies by Pouransari & Mani (2017) and Rahmani *et al.* (2015) showed that preferential concentration can have a significant impact on the particle temperatures while having little effect on the mean gas temperature rise. While these studies demonstrated the relevance of some of the multiphysic processes in play, they ignored the effect of particle shadowing or radiation attenuation by adopting an optically thin model. Also, they did not account for real effects in practical applications such as the presence of walls, or turbophoresis (Reeks 1983). In addition to the scarcity of studies exploring the complete physics of particle-turbulence-radiation interactions, there is a lack of experimental data providing evidence of the impact of preferential concentration on radiation transmission and absorption to be used for validation of such studies, or the reduced order models that may stem from them.

We present an experimental study in which a fully developed particle-laden turbulent flow of air confined in a square duct is exposed to monochromatic near-infrared radiation. The flow regime and particle characteristics are chosen such that the particle-turbulence interaction induces large fluctuations in the particle concentration field and that the rise in gas temperature is measurable. We analyze the effect of particle loading on the mean gas temperature rise and the radiation attenuation. For the studied range of mass loading ratios, the corresponding volume loadings are still within the dilute regime, and it is considered that variations of particle loading do not alter the particle preferential concentration through turbulence modulation. A one-dimensional heat transfer model is used to analyze the dependence of the mean gas temperature on flow and particle parameters. Comparing the result of this model against experimental measurements shows the importance of radiation attenuation as the particle loading increases. The results also underscore the impact of walls that lead to regions of high particle concentration and low velocity. Near-wall phenomena may compromise the performance of the system and impose safety constraints such as maximum wall temperature service limits.

The report is organized as follows. Section 2 describes the experimental setup, the particle and flow parameters and the measurement techniques. Results are presented in Section 3 and divided into four subsections where we discuss the impact of particle, flow and radiation parameters based on the one-dimensional model, wall-normal distributions of particle concentration and velocity at the duct center, radiation attenuation, and gas temperature rise results. Conclusions are drawn in Section 4.

2. Experimental methods

Experiments were performed in a vertical square duct air flow facility at Stanford University. A fully developed particle-laden turbulent flow was exposed to radiation in a glass test section. The open loop wind tunnel and the test section are pictorially described in Figure 1.

The flow is driven by a variable speed centrifugal pressure blower operated by a closed loop controller to maintain a constant Reynolds number, which is computed based on the duct width, bulk velocity and kinematic air viscosity at the test section. Particles are injected into a flow conditioning section by a volumetric screw feeder and dispersed

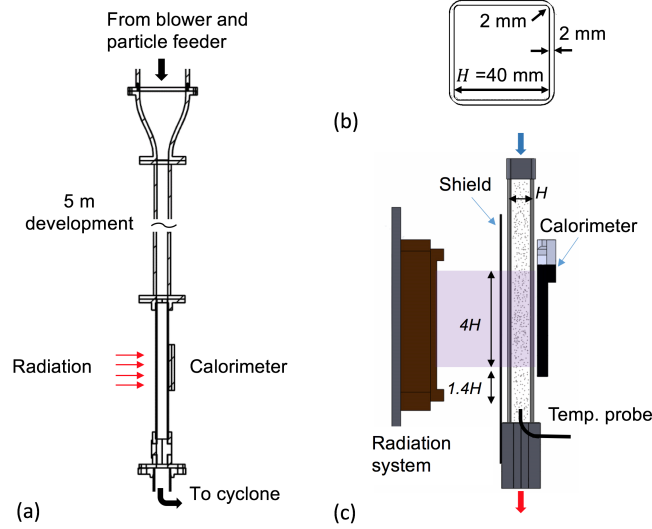


FIGURE 1. Experimental apparatus: (a) layout of the particle-laden duct flow facility, (b) test cross-section, and (c) test section sketch including the radiation source and the thermal measurement techniques (calorimeter and thermocouple probe).

laterally via several grids. The particle-air mixture is accelerated through a 16:1 contraction as it enters the flow development section. A 5.4 m-long smooth aluminum duct, with a 40 mm-wide internal square cross-section, ensures that fully developed conditions are reached for the flow and particles at the test section. The test section is a 425 mm-long duct made of borosilicate glass, with a wall thickness of 2 mm, and a nominal internal cross-section of 40 mm \times 40 mm. The cross-section deviates from a perfect square in the 2 mm internal corner radii, a consequence of the extrusion process used to manufacture the test section [Figure 1(b)]. Extruded glass presents the advantage of eliminating joints that are more sensitive to failure under strong radiation. Particles are recycled at a cyclone separator downstream of the test section.

The radiation source is a High Power VCSEL (Vertical-Cavity Surface-Emitting Laser) array manufactured by Princeton Optronics Inc., that provides near-collimated radiation at a wavelength of 975 nm. The emitting surface is located parallel to one of the test section walls, at about 11 cm from it, and produces a tall, wide beam. This beam is masked by a shield right in front of the test section to a window of the same width as the test section and a streamwise length of 160 mm [Figure 1(c)].

All experiments were performed at a Reynolds number of $Re_H = 20,000 \pm 0.7\%$. Nearly spherical nickel particles with a number-based mean diameter of $11.8 \pm 0.5 \mu\text{m}$ were used in the experiments. Particle-size distributions measured with a Coulter Counter showed a relatively narrow distribution with low-probability tails that covered a range from about 6 to 20 μm . Comparison of size distributions of particle samples before and after the tests (recovered at the cyclone) demonstrated that their sizes were not selectively filtered by the rig. The averaged Stokes number, based on the mean particle diameter and the flow Kolmogorov time scale computed from the channel-averaged dissipation rate, is $\overline{St}_\eta = 12$. Experiments were performed at different mass loading ratios, Φ , defined as the ratio of the mass flow rate of particles to the mass flow rate of air. Loadings were varied from $\Phi = 0.025$ to 0.4, with a maximum uncertainty on the mean value of 0.004 that decreases for increasing loadings. Despite the moderate mass loading ratios, the particle volume

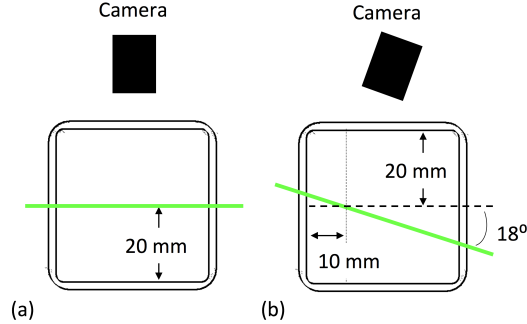


FIGURE 2. Laser sheet configurations used for measurements of: (a) particle velocity and concentration at the central plane of the duct, (b) mean concentration near the wall.

fraction remained under $O(10^{-4})$. The radiation source provided a total power of $1 \text{ kW} \pm 2\%$ across the radiation shield. The measured transmission through the 2 mm-thick borosilicate walls and for the particular radiation wavelength was $92.4\% \pm 0.3\%$, leaving the gas-particle mixture nominally exposed to a radiation of about 924 W.

Optical measurements of the particle-phase velocity and concentration were made in the absence of heating to evaluate the inlet conditions to the radiated section. Two-dimensional Particle Image Velocimetry (PIV) techniques were used to obtain mean streamwise particle velocities at the central test section plane from 2000 image pairs. The estimated uncertainty on the mean velocity is lower than 0.3%. Measurements of particle concentration used the two-dimensional coordinates of the particle centroids obtained from the same dataset, but using only one of the images from each PIV pair. The field of view is limited in the vicinity of the lateral walls by the rounded corners of the test section. An angled laser sheet configuration was adopted to measure the concentration distribution near the wall. In this latter case, the laser sheet is inclined 18° with respect to the wall-normal and it crosses the central plane of the test section at 10 mm from the wall, as sketched in Figure 2(b). The laser sheet width, defined as the $1/e^2$ Gaussian beam width, was 1.6 mm for the inclined configuration and 1.4 mm for the wall-normal configuration. In both cases, the laser width was uniform along the complete camera field of view, and the height of the laser sheet in the streamwise direction was about 25 mm. Figure 2 pictures the laser sheet configurations used for the optical measurements in the central plane (a), and near the walls (b).

Total transmitted power and mean gas temperature rise were evaluated for varying particle loadings. A black-coated water-cooled copper calorimeter facing the radiation source at the opposite side of the test section provided the total transmitted power with an uncertainty of $\pm 10 \text{ W}$. This uncertainty was estimated based on the measurement uncertainties of the flow-rate of water through the calorimeter and its temperature rise. The mean gas temperature was measured with a custom-made thermocouple probe with wires perpendicular to the flow direction and supported by two thin prongs mounted in a L-shaped stem. The butt-welded K-type thermocouple has a diameter of $75 \mu\text{m}$ and a half-length of 2.5 mm. The probe was traversed along the wall bisector from the center of the duct towards the radiation source, at a downstream distance of 55 mm in the streamwise direction from the exit of the radiated section. This separation was required to avoid errors due to scattered radiation to the thermocouple. The estimated uncertainty in the measurement of the temperature rise is $0.2 \text{ }^\circ\text{C}$.

3. Results

We first analyze the effect of various parameters on the particle and gas temperature using a simplified one-dimensional model. Then, results are presented for the particle velocity and concentration distributions across the test section, gas temperature profiles, and total radiation attenuation.

Particle-turbulence-radiation interactions in confined flows are not homogeneous or isotropic, rendering even more complex its comprehensive parametric study. To analyze the effect of shear, turbophoresis and wall-heat transfer, the experimental data are contrasted to the predictions from the one-dimensional model in the optically thin limit, and to the Beer-Lambert law for transmission attenuation.

3.1. One-dimensional model

We consider an optically transparent rectangular duct exposed to collimated radiation through one of the walls, as in the experiment. We assume the number density of particles to be known and uniform in space, the volume fraction to be small, and that particles and gas move together at the bulk velocity, neglecting turbulent fluctuations. An energy balance on a differential control volume gives a system of coupled ordinary differential equations for the fluid and particle temperature that are

$$\rho_f c_{p,f} U \frac{dT_f}{dx} = n h_p A_p (T_p - T_f), \quad (3.1)$$

$$\rho_p c_{p,p} V_p U \frac{dT_p}{dx} = -h_p A_p (T_p - T_f) + \sigma_{abs} A_{pc} I. \quad (3.2)$$

Here, x and y denote the streamwise and wall-normal directions, respectively, while the subscripts f and p refer to the fluid and particle phases. Density is denoted by ρ , c_p is the specific heat, U is the bulk velocity, T is temperature, n is the particle number density, h_p is the particle to gas convective heat transfer coefficient, σ_{abs} is the absorption coefficient of radiation, and I is the radiation intensity seen by a particle. A_p , V_p and A_{pc} are particle geometrical parameters referring to the surface area, volume and projected cross-sectional area, respectively. Note that by neglecting turbulent and diffusive transport, Eqs. (3.1)-(3.2) are also valid if variables change in the wall-normal direction, giving a quasi one-dimensional model [e.g., $U(y)$, $n(y)$, $T(y)$, $I(y)$].

We define the following non-dimensional variables by analogy to the conventional analysis of heat transfer in a pipe flow

$$T^* = \frac{T - T_o}{T_o}, \quad x^* = \frac{x}{H RePr}, \quad I^* = RePr \frac{H}{L} \frac{\tau_{flow}}{\tau_{rad}} \frac{I}{I_o},$$

$$\gamma = RePr \frac{H}{L} \frac{\tau_{flow}}{\tau_{p,t}} \frac{c_{p,p}}{c_{p,f}}, \quad \beta = \gamma \left(\Phi + \frac{c_{p,f}}{c_{p,p}} \right),$$

where T_o is the inlet temperature, L the heated section, $\tau_{flow} = L/U$ is the flow through time, $\tau_{p,t} = (\rho_p c_{p,p} V_p) / (h_p A_p)$ is the particle thermal time constant, and $\tau_{rad} = (\rho_p c_{p,p} V_p T_o) / (\sigma_{abs} A_{pc} I_o)$ is the time for radiation to approximately double the initial particle temperature. No assumption is made on the attenuation of the radiation intensity. In the so-called optically thin limit, the intensity is assumed constant across the domain and equal to the incoming radiation intensity I_o . This approximation holds true for very low particle volume loadings. As the loading increases, particles deeper into the medium experience lower radiation intensity due to attenuation by particles located closer to the source. The previous system of equations has the following solution in the

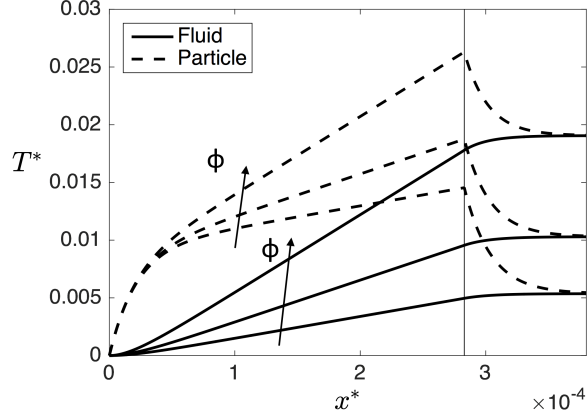


FIGURE 3. Evolution of non-dimensional particle and fluid temperatures in the streamwise direction at different mass loading ratios, $\Phi = 0.1, 0.2,$ and 0.4 . The vertical line denotes the end of the heated section.

heated section in non-dimensional form

$$T_p^* - T_f^* = \beta^{-1} I^* \left(1 - e^{-\beta x^*} \right), \quad (3.3)$$

$$T_f^* = \frac{\Phi}{\Phi + c_{p,f}/c_{p,p}} I^* x^* - \frac{\Phi}{\Phi + c_{p,f}/c_{p,p}} \beta^{-1} I^* \left(1 - e^{-\beta x^*} \right). \quad (3.4)$$

In the presence of turbulent fluctuations, this solution can be interpreted in terms of phase-averaged temperatures in the wall-normal direction (or mixed mean temperatures), and it would be exact if turbulent mixing could be neglected.

Equations (3.3)-(3.4) show that after a short development length, the particles and fluid achieve a constant temperature difference, and the temperature of both phases then increases linearly in the streamwise direction. This regime can be considered thermally fully developed by analogy to the thermally developed state in pipe flows with constant wall-heat flux. Equation (3.4) reflects different regimes for the dependence of the rate of fluid temperature rise with the mass loading. After an initial transient at the entrance of the heated section, the fluid temperature rise along the streamwise direction, $dT_f^*/dx^* \sim \Phi/(\Phi + c_{p,f}/c_{p,p})$ is approximately linear with loading, for small Φ . Note that the ratio of specific heat capacities is approximately 2 for nickel particles and air. As the mass loading increases and Φ becomes of $O(1)$, the fluid temperature rise becomes a non-linear function of Φ , and it reaches saturation at even larger loadings. This saturation is the result of $T_p^* - T_f^* \propto \beta^{-1}$ in Eq. (3.3), that suggests an inverse relationship between $T_p^* - T_f^*$ and Φ . However, note that the model loses its accuracy as the loading increases, where additional effects such as two-way coupling and particle collisions become important.

The solutions of the above equations for the experimental conditions in the duct center at the three tested mass loadings are shown in Figure 3. The temperature solutions are extended up to 55 mm downstream of the heated section, where the gas temperatures were measured. The same set of equations was solved in this region by setting $I^* = 0$ and matching conditions at the interface. In the absence of external radiation, the particle temperature decrease is more significant than the marginal increase experienced by the gas temperature. The particle and fluid temperatures reach equilibrium at the measurement location.

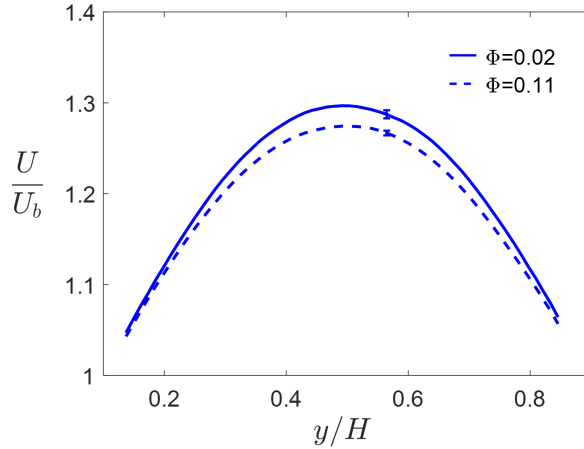


FIGURE 4. Mean streamwise particle velocity along the wall bisector normalized by the bulk velocity for two mass loading ratios, $\Phi = 0.02$ and 0.1 .

We can use this one-dimensional model to compare the particle-based solar receiver concept described in the introduction to a conventional solar receiver in which the working fluid is heated by absorbing walls. One possible approach is to define the equivalent Nusselt number that would be required in the conventional system to provide the same fluid temperature rise when the four walls are heated to the same temperature as the particles in the particle-based solar receiver. Considering the fully developed thermal state, the expression for the equivalent Nusselt number in terms of the variables defined for the one-dimensional model is given in Eq. (3.5). Using the experimental values, a $\text{Nu}_{\text{equiv}} \approx 450$ is required to obtain the same particle to fluid heat flux as in the experiments for $\Phi = 0.1$. For comparison, the Nusselt number for a thermally fully developed turbulent pipe flow in air at a Reynolds number of $\text{Re} = 20,000$ is $\text{Nu} \approx 50$. This analysis indicates that a much higher wall temperature would be required in a conventional solar receiver to achieve the particle to fluid heat flux provided by a particle-solar receiver.

$$\text{Nu}_{\text{equiv}} \equiv \frac{H}{k_f} \left(\frac{q''}{T_p - T_f} \right) = \frac{1}{4} \gamma \Phi \approx 4500\Phi. \quad (3.5)$$

3.2. Unheated conditions

The heat transfer from particles to gas and the gas temperature rise are affected by the particle number density field and the velocity of the particles. Therefore, variations of mean particle concentration and velocity across the test section result in a non-uniform gas temperature. In addition, the experimental analysis of radiation absorption from measurements of gas temperature rise relies on the knowledge of these two variables. The particle phase was characterized via unheated experiments, that provided the inlet conditions to the radiated section. Owing to the mild temperature rises measured for the present experimental conditions, mean particle velocities and concentrations can be considered unaltered in the presence of radiation.

We used two-dimensional PIV to measure mean particle streamwise velocities at the central plane of the test section, and hot-wire anemometry to measure the unladen streamwise gas velocity along the wall-normal direction. The particle slip velocity is smaller than the PIV velocity resolution, thus yielding particle and gas velocities that are equal within the measurement uncertainty. Wall normal profiles of particle velocities

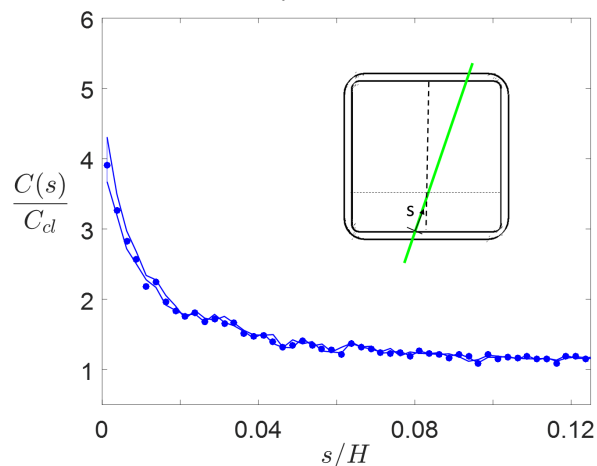


FIGURE 5. Non-dimensional mean particle concentration distribution along the beam direction, s coordinate, of a planar laser sheet inclined 18° with respect to the wall-normal. The distribution of mean concentration in the vicinity of the wall is normalized by the mean concentration at the intersection between the inclined illumination plane and the wall bisector, at $H/4$ from the wall. Results correspond to a mass loading ratio lower than 0.01.

at the duct center plane are shown in Figure 4 for two mass loadings. Mean velocities are higher than the bulk velocity in the central 75% of the test section width covered by the camera field of view. The variation of velocity within this region translates into different particle residence times in the radiated section, inducing a variation in the mean gas temperature. The effect of varying mass loading on the mean velocity is measurable but small, causing a maximum velocity difference lower than 2%.

Variations in the mean particle number density also affect the gas temperature distribution, and in addition, they impact the attenuation of the radiation as it penetrates into the particle-gas mixture. In wall-bounded particle-laden turbulent flows, gradients in the wall-normal fluctuating fluid velocity are known to cause particles to drift towards the walls (Guha 2008). This phenomenon is referred to as turbophoresis. The inclined laser sheet configuration shown in Figure 2(b) was adopted to quantify the increase of concentration near the walls. Figure 5 shows the concentration profile along the inclined plane made non-dimensional by its value at the intersection between the central and inclined planes. The measurements were done at a low mass loading ratio, less than 1%, that was required in order to accurately identify individual particles near the wall. Coordinates of particle centroids were identified in over 2000 images to compute the average number of particles in bins of 0.1 mm in the laser beam direction. Particle concentrations are not experimentally accessible in the near-wall region, under a y^+ of 1, as a consequence of the dead volume arising from the intersection of the inclined finite width laser sheet with the wall. The mean concentration drops quickly in the first 1 mm from the closest wall measurement location, length that corresponds to less than 2.5% of the duct width, and it plateaus after approximately 3 mm, or 7.5% of the duct width. Thus, the number density of particles was uniform across most of the test section in the present experiments, justifying our earlier assumption in the one-dimensional model. Note that at higher loadings, inter-particle collisions become important, reducing turbophoresis and relative concentrations of particles near the wall, and leading to more uniform mean particle concentrations.

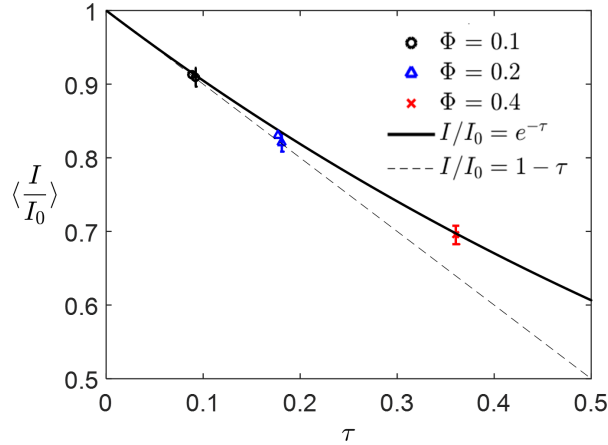


FIGURE 6. Attenuation of total transmitted radiation across the test section as a function of optical depth. Symbols are experimental data, and repeated points indicate repeated experiments. The solid line is the Beer-Lambert law and the light dashed line is the optically thin approximation.

Instantaneous snapshots of the particle density field demonstrated the existence of preferential concentration for the current experimental conditions. The sensitivity of preferential concentration to mass loading and Reynolds number variations in the present experiments was analyzed by Villafaña *et al.* (2016). The authors reported a small decrease of the strength of preferential concentration when the mass loading ratio was varied from 0.024 to 0.12. However, they acknowledged the sensitivity of metrics computed from planar optical techniques to the number of particles due to particle overlapping in the two-dimensional images.

3.3. Radiation transmission

The total transmitted radiation through the particle-gas mixture was inferred from the measurements of the radiation power incident on the calorimeter. The attenuation caused by the borosilicate walls as the radiation travels from the diode array to the calorimeter was accounted for by measuring the transmitted radiation with particles and then immediately after without particles in the flow. The ratio of these two measurements cancels the effect of the glass attenuation and represents the attenuation caused by the particles. The averaged radiation attenuation by the particles across the channel, integrated along the full radiated section, is shown in Figure 6 for the three tested mass loading ratios. The attenuation is plotted as a function of optical depth, $\tau = \sigma_{ext} A_{pc} n H$, which would be proportional to the mass loading ratio Φ , under the assumption of uniform number density. The extinction coefficient accounts for the extinction due to absorption and scattering and was obtained from tabulated values using the complex index of refraction from Mie scattering calculations.

The solid line in Figure 6 represents the exponential decay of transmitted radiation through a medium with optical depth τ predicted by the Beer-Lambert law, neglecting scattering and black body emission. To within experimental error, and keeping into account that the number density and the extinction coefficient are estimated values, the data show good agreement with the Beer-Lambert law. This agreement indicates that preferential concentration is not affecting the total transmitted radiation in a major way.

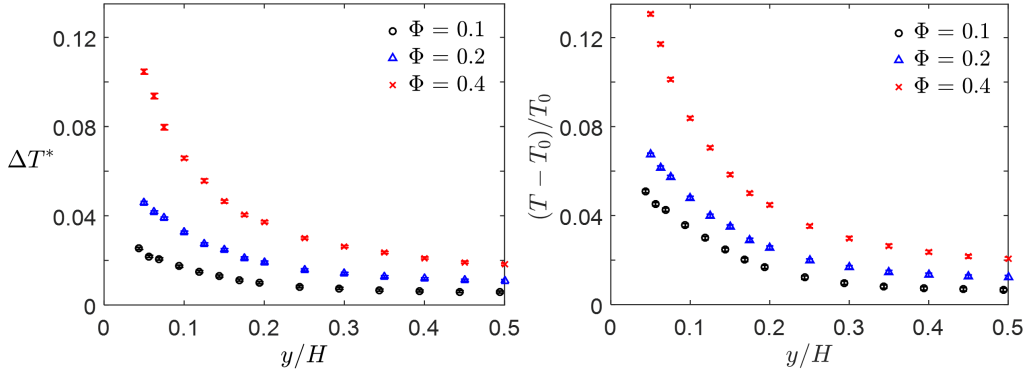


FIGURE 7. Non-dimensional gas temperature rises along the wall bisector parallel to the direction of radiation, downstream of the radiated section. (a) Particle contribution, computed by subtracting the gas temperatures with and without particles, divided by the unheated inlet temperature. (b) Particle and wall contributions, computed by subtracting the unheated inlet temperature from the gas temperatures in the presence of particles, divided by the unheated inlet temperature.

However, due to its large size, the calorimeter not only represents the fraction of the incident power that is directly transmitted through the mixture, but also collects radiation scattered by the particles and reflected by the lateral walls. These additional contributions could be shadowing the expected decrease in attenuation caused by particle clustering. If the medium was optically thin, each particle would be exposed to the same radiative heat flux and the total transmitted power normalized by the irradiated area would obey the linear decay shown by the dashed line. The two lowest loadings are reasonably approximated by the optically thin assumption, whereas deviations are clear at $\Phi = 0.4$.

3.4. Gas temperature rise

Mean gas temperatures were measured along the wall bisector parallel to the direction of radiation, across the half of the test section width closest to the diode array. Radiation absorption by the walls adds further complexity in wall-bounded applications since the gas temperature rise is also affected by wall-to-fluid heat transfer.

In order to evaluate the temperature rise caused only by the particles, temperature profiles were measured with and without particles and subtracted. In reality the contributions of walls and particles to the temperature rise do not obey a linear superposition (Kuersten *et al.* 2011), and so this decomposition is only approximate. Figure 7(a) plots the ratio of the temperature rise due to particles to the inlet temperature for the three tested mass loadings. The gas temperature rise increases with increasing mass loading and towards the wall owing to higher residence time. Note that the particle concentration is uniform in the region where the gas temperatures were measured. The temperature rise at the location closest to the wall relative to that at the center increases significantly with increasing mass loading.

Subtracting the inlet temperature from the gas temperatures in the presence of particles provides the total gas heating due to the particles and wall heat transfer [Figure 7(b)]. This ratio can be interpreted as a Boussinesq parameter. At the highest loading, this quantity reaches values over 0.12 at about 4 mm from the wall, indicating that buoyancy coupling may become important near the walls. Comparison of the gas temperature

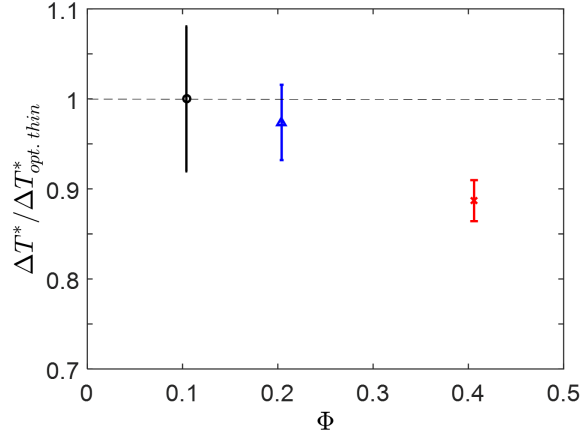


FIGURE 8. Non-dimensional gas temperature rise at the duct centerline as a function of mass loading ratio. Gas temperature difference with and without particles in the flow is normalized by the one-dimensional optically thin model prediction.

rises caused by the particles [Figure 7(a)] with those caused by the particles and the wall [Figure 7(b)] shows that while for the lowest loading the gas temperature rise is mostly dominated by the wall, at the highest loading particle-to-gas heat transfer is the dominant effect.

The accuracy of the one-dimensional model using the optically thin assumption is examined in Figure 8, by computing the ratio of the measured temperature rise at the duct center to the model prediction. The model uses the measured particle velocity at the duct center. The normalized temperature difference decreases with mass loading, in agreement with the decrease in attenuation observed for the radiation transmission results when compared to the attenuation in an optically thin medium. At higher loadings, particles become partially shadowed and experience less radiative flux, resulting in reduced temperatures.

Figure 9 uses this same optically thin temperature rise at the duct center to rescale the profiles of gas temperature rise caused by the particles. Overall, the profiles are reasonably collapsed despite small deviations for the highest loading close to the wall. The overlapping reflects that for the mass loadings analyzed, the increase in optical depth and corresponding attenuation along the radiation path are not yet significantly large as to induce large modifications on the shape of the wall-normal temperature rise profiles.

4. Conclusions

Radiation absorption by inertial particles dispersed in a turbulent square duct flow was examined experimentally, and the results were compared to the predictions of a one-dimensional optically thin model. While the optically thin scaling accounts for most of the variation in temperature rise as a function of mass loading ratio, small deviations due to optical depth start to become apparent at the highest loading. Also, despite the presence of preferential concentration, transmission results are in good agreement with the exponential decay predicted by the Beer-Lambert law for a uniform absorbing medium. Future work will examine the effect of preferential concentration on the temporal fluctuations in the transmitted radiation and gas temperature.

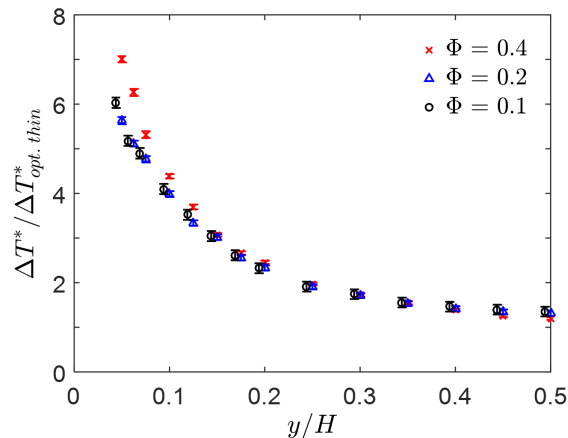


FIGURE 9. Non-dimensional gas temperature rise due to particles along the wall bisector for different mass loading ratios normalized by the one-dimensional optically thin model prediction at the center of the duct.

Acknowledgments

This investigation was funded by the Advanced Simulation and Computing (ASC) program of the US Department of Energys National Nuclear Security Administration via the PSAAP-II Center at Stanford, Grant No. DE-NA0002373-1.

REFERENCES

- BERTOCCHI, R., KARNI, J. & KRIBUS, A. 2004 Experimental evaluation of a non-isothermal high temperature solar particle receiver. *Energy* **29**, 687–700.
- BRIAN, P., HALES, H. & SHERWOOD, T. 1969 Transport of heat and mass between liquids and spherical particles in an agitated tank. *AIChE J.* **15**, 727–733.
- CASADAY, B., PRENTER, R., BONILLA, C., LAWRENCE, M., CLUM, C., AMERI, A. A. & BONS, J. P. 2014 Deposition with hot streaks in an uncooled turbine vane passage. *J. Turbomach.* **136**, 041017.
- CHEN, H., CHEN, Y., HSIEH, H. & SIEGEL, N. 2007 Computational fluid dynamics modeling of gas-particle flow within a solid-particle solar receiver. *J. Sol. Energy Eng.* **129**, 160–170.
- CROCKER, A. & MILLER, F. 2011 Coupled fluid flow and radiative modeling for a small particle solar receiver. *AIAA Paper #* 2011-5902.
- FESSLER, J., KULICK, J. & EATON, J. K. 1994 Preferential concentration of heavy particles in a turbulent channel flow. *Phys. Fluids* **6**, 3742–3749.
- GUHA, A. 2008 Transport and deposition of particles in turbulent and laminar flow. *Annu. Rev. Fluid Mech.* **40**, 11–41.
- KIM, K., SIEGEL, N., KOLB, G., RANGASWAMY, V. & S.F, M. 2009 A study of solid particle flow characterization in solar particle receiver. *Sol. Energy* **83**, 1784–1793.
- KLEIN, H., RUBIN, R. & KARNI, J. 2008 Experimental evaluation of particle consumption in a particle seeded solar receiver. *J. Sol. Energy Eng.* **130**, 011012.
- KOSTINSKI, A. B. & SHAW, R. A. 2001 Scale-dependent droplet clustering in turbulent clouds. *J. Fluid Mech.* **434**, 389–398.

- KUERTEN, J., VAN DER GELD, C. & GEURTS, B. 2011 Turbulence modification and heat transfer enhancement by inertial particles in turbulent channel flow. *Phys. Fluids* **23**, 123301.
- LENERT, A. & WANG, E. 2012 Optimization of nanofluid volumetric receivers for solar thermal energy conversion. *Sol. Energy* **86**, 253–265.
- MATSUDA, K., ONISHI, R., HIRAHARA, M., KUROSE, R., TAKAHASHI, K. & KOMORI, S. 2014 Influence of microscale turbulent droplet clustering on radar cloud observations. *J. Atmos. Sci.* **71**, 3569–3581.
- MATSUDA, K., ONISHI, R., KUROSE, R. & KOMORI, S. 2012 Turbulence effect on cloud radiation. *Phys. Rev. Letters* **108**, 224502.
- MILLER, F. & KOENIGSDORFF, R. 2000 Thermal modeling of a small-particle solar central receiver. *J. Sol. Energy Eng.* **122**, 23–29.
- MAXEY, M. R. 1987 The gravitational settling of aerosol particles in homogeneous turbulence and random flow fields. *J. Fluid Mech.* **174**, 441–465.
- POURANSARI, H. & MANI, A. 2017 Effects of preferential concentration on heat transfer in particle-based solar receivers. *J. Sol. Energy Eng.* **139**, 021008.
- RAHMANI, M., GERACI, G., IACCARINO, G. & MANI, A. 2015 Polydisperse particles in an irradiated turbulent gas-particle mixture. *Annual Research Briefs*, Center for Turbulence Research, Stanford University, 27–41.
- REEKS, M. 1983 The transport of discrete particles in inhomogeneous turbulence. *J. Aerosol Sci.* **14**, 729–739.
- SHAW, R., KOSTINSKI, A. & LANTERMAN, D. 2002 Super-exponential extinction of radiation in a negatively correlated random medium. *J. Quant. Spectrosc. Ra.* **75**, 13–20.
- SQUIRES, K. D. & EATON, J. K. 1991 Preferential concentration of particles by turbulence. *Phys. Fluids A* **3**, 1169–1179.
- SUNDARAM, S. & COLLINS, L. 1997 Collision statistics in an isotropic particle-laden turbulent suspension. part 1. direct numerical simulation. *J. Fluid Mech.* **335**, 75–109.
- VILLAFANE, L., ESMAILY-MOGHADAM, M., BANKO, A. & EATON, J. K. 2016 A robust method for quantification of preferential concentration from finite number of particles. *Annual Research Briefs*, Center for Turbulence Research, Stanford University, 123–135.
- WILLIAMS, F. A. 1958 Spray combustion and atomization. *Phys. Fluids* **1**, 541–545.
- YAPA, S., ELKINS, C. & EATON, J. K. 2015 Quantitative MRI measurements of hot streak development in a turbine vane cascade. *ASME Turbo Expo*, GT2015-42767.
- ZAMANSKY, R., COLETTI, F., MASSOT, M. & MANI, A. 2014 Radiation induces turbulence in particle-laden flows. *Phys. Fluids* **26**, 071701.